PHYSICAL REVIEW A VOLUME 55, NUMBER 2 FEBRUARY 1997

Photon correlation spectroscopy of the Jaynes-Cummings system

B. C. Sanders,[1,2] H. J. Carmichael,[1] and B. F. Wielinga[2]
[1]*Department of Physics, University of Oregon, Eugene, Oregon 97403-1274*
[2]*School of Mathematics, Physics, Computing and Electronics and Centre for Lasers and Applications,*
Macquarie University, North Ryde, New South Wales 2109, Australia

(Received 9 August 1996)

The spectroscopic detection of the excited-state resonances of a strongly coupled atom and optical cavity mode is complicated by inhomogeneous broadening, due to the variation of the dipole coupling constant with location in the cavity. Photon correlation spectroscopy circumvents the difficulty for slowly moving atoms using frequency-selective two-photon absorption and photon coincidence detection of the two-photon decay. [S1050-2947(97)04501-0]

PACS number(s): 42.50.Ct, 42.50.Dv

I. INTRODUCTION

The Jaynes-Cummings model provides a simple description of a two-level atom interacting with one mode of the quantized electromagnetic field [1,2]. It is a basic model of theoretical quantum optics and has been studied extensively over a period of some thirty years. The large theoretical literature which has grown on the subject is focused on physics which has an explicit origin in the quantized nature of the electromagnetic field [3,4]. From it, one would hardly discern that Jaynes and Cummings were themselves quite skeptical about detecting differences between their quantum-mechanical model and the corresponding semiclassical theory; in their evaluation [1]: ‘‘ . . . the prospects of detecting such a difference are extremely dubious, for we will see that the semiclassical theory actually reproduces many of the features which one commonly supposes can be found only with field quantization.’’ The detection of a difference was, in fact, claimed within a decade of Jaynes and Cummings work [5], and over the next few years the differences grew into what is now the familiar collection of nonclassical effects in resonance fluorescence [6]. We should note, however, that resonance fluorescence involves rather different physics from that addressed in Jaynes and Cummings’ original paper. The latter is concerned with coherent quantum evolution, evolution in the absence of dissipation. Nonclassical effects in resonance fluorescence involve irreversible processes: radiation into free space and the detection of that radiation by the photoelectric effect. In a more accurate commentary then, resonance fluorescence demonstrates departures from the multimode extension of semiclassical theory developed by Jaynes and his students [7,8]. In this sense the challenge of Jaynes and Cummings’ original paper remains to be met.

The issue on which the challenge turns is that of entanglement, as is made clear in the following passage [1]: ‘‘ . . . for in the semiclassical equations the ‘‘driving term’’ appears as $\langle H'\rangle\langle E\rangle$, while quantum electrodynamics yields $\langle H'E\rangle$. The difference between these terms arises from the possibility of having correlated states, ... This possibility forms the basis of one of Einstein’s objections to quantum mechanics. . . . An interesting line of thought is based on the fact that the semiclassical theory and quantum electrodynamics predict different equations of motion for the molecule in the field, the difference arising just from those correlated states which cause the above conceptual difficulties. Thus if one could find any experimental situation in which the difference between $\langle H'E\rangle$ and $\langle H'\rangle\langle E\rangle$ leads to an observable difference in maser observations, this would constitute an indirect, but convincing, check on those aspects of quantum theory which lead to the Einstein-Podolsky-Rosen paradox.’’

Today, discussions of entanglement focus on the nonlocal correlations emphasized in the work of Bell [9,10]. The distinction Jaynes and Cummings draw, between $\langle H'\rangle\langle E\rangle$ and $\langle H'E\rangle$, does not concern nonlocal correlations *per se*. Perhaps, however, it comes even closer to the fundamental role of entanglement in quantum mechanics, the implications of which are addressed through spectroscopy. According to quantum mechanics, a strongly coupled atom and cavity mode is not merely *an atom* exchanging energy with *a cavity mode*; this is the conception in semiclassical theory. In quantum mechanics the atom and cavity mode become entangled; they form a composite entity, with stationary states that are entangled states, and characteristic transition frequencies between these states. It would be difficult to overstate the importance of this idea—an idea which entered quantum mechanics as the theoretical basis of the atomic spectroscopy which established the subject and is central to so much of our understanding in molecular, condensed matter, and particle physics. In the case of the Jaynes-Cummings system, the spectroscopy follows from a nonperturbative calculation in QED and is the foundation on which all work in nonperturbative cavity QED is built.

This paper is concerned with the experimental possibilities for measuring the Jaynes-Cummings spectrum. Measurements have been pursued for nearly a decade. The first was performed on a beam of Rydberg atoms traversing a superconducting microwave cavity [11] in a close realization of the maser configuration considered in Jaynes and Cummings’ work [1]. The experiment is operated in the time domain where the collapse and revival of Rabi oscillations provides the spectral information. A refined microwave experiment has recently extracted distinct frequencies from the Rabi oscillation signal [12] and produced the first quantitative results on the excited states of the Jaynes-Cummings system. Experiments at optical frequencies have also been performed, and here one can observe absorption and emission lines directly in the frequency domain. The experiments have not yet achieved equivalent success, however. The ground to first excited-state absorption has been observed [13–15], and the spectrum is a doublet, the so-called vacuum Rabi spectrum. But the doublet is generic, not a distinguishing feature of the Jaynes-Cummings Hamiltonian; it arises from normal modes wherever the electric field and material polarization are strongly coupled in the linear optics regime. A similar linear response is observed in semiconductor microcavities where the normal modes are identified as cavity polaritons [16]. Here the behavior is clearly semiclassical [17] and the nonlinear spectroscopy [17–22] certainly differs from that which is derived from the Jaynes-Cummings Hamiltonian.

The advantage of microwave frequencies over optical frequencies comes from the larger wavelength and period of microwave radiation. Experiments to date use atomic beams. The Jaynes-Cummings spectrum depends on the dipole coupling constant, which depends, in turn, on the location of the atom in the cavity mode. In a standing-wave cavity, it is necessary, therefore, to confine the transverse width of the atomic beam on the scale of the radiation wavelength. This is a relatively easy task at microwave frequencies but very difficult for optical fields. The motion of the atoms through the cavity mode is also a problem. If the probability of photon loss during the transit time is negligible, the accumulated Rabi phase is simply the integral of the time-varying coupling constant. Such is the case at microwave frequencies, where the photon lifetime is many times longer than the transit time through the Gaussian mode [11,12]. At optical frequencies, however, although the cavity Q may be higher [15], the absolute photon lifetime is generally shorter than the transit time of the atoms; the spontaneous emission lifetime is even shorter still. Under these conditions, the Rabi oscillation of a typical atom is interrupted by photon emission at many different locations across the Gaussian mode. A complicated combination of homogeneous and inhomogeneous broadening of the spectrum results.

We recently proposed a technique for overcoming these difficulties [23] without adopting the extreme idealization of localizing an atom on the scale of the optical wavelength. Our proposal holds for cooled or slowed atomic beams for which a quasistatic approximation may be made. For sufficiently slow atoms, radiative equilibrium is reached with an essentially fixed dipole coupling constant, $g(\boldsymbol{r})$, at every point along an atom's path. The broadening is then entirely inhomogeneous and accounted for by a distribution over $g(\boldsymbol{r})$. The proposed technique, *photon correlation spectroscopy*, selectively excites a subensemble of Jaynes-Cummings systems, having $g(\boldsymbol{r})$ within a narrow band, by resonant two-photon absorption in a coherent bichromatic field—a hole-burning approach. The excitation decays with the emission of two photons, thus enabling a measurement of the absorption resonances by the detection of two photons in coincidence as one frequency of the bichromatic field is swept. Simulations of an experiment using quantum trajectory methods demonstrate the feasibility of this technique [23]. The simulations include the corrections to the quasistatic approximation and various other details of an actual experiment. They use a great deal of computer time, however. In this paper we therefore develop an alternate approach, valid in the exact quasistatic limit [24]. We solve the master equation for one atom coupled to a cavity mode with fixed $g(\boldsymbol{r})$ and driven by a bichromatic field. Inhomogeneous broadening is incorporated by averaging against the distribution, $P[g(\boldsymbol{r})]$, of the dipole coupling constant for a uniform spatial distribution of the atom and a standing-wave TEM_{00} mode function. Implementing this approach uses a small fraction of the computer time, thereby making a search for optimal experimental conditions feasible.

In Sec. II the photon correlation spectroscopy technique is outlined in physical terms. Its theoretical implementation for the quasistatic limit is developed in Sec. III where the master equation for the Jaynes-Cummings system with radiative linewidths and bichromatic excitation is solved. The photon coincidence spectra obtained from this solution are discussed in Sec. IV, first without inhomogeneous broadening and then after averaging over the distribution of dipole coupling constants; the two distributions used to take the average are derived in an Appendix. Our conclusions are given in Sec. V.

II. PHOTON CORRELATION SPECTROSCOPY

A. The Jaynes-Cummings spectrum

The Jaynes-Cummings model describes the resonant, or near-resonant interaction, via an atomic dipole transition, of one atom and one quantized mode of an electromagnetic cavity. The resonance condition allows the atom to be treated as a two-level system with raising, lowering, and inversion operators $\hat{\sigma}_+$, $\hat{\sigma}_-$, and $\hat{\sigma}_3$, respectively. The electromagnetic field mode has annihilation and creation operators $\hat{a}$ and $\hat{a}^\dagger$, and the Jaynes-Cummings Hamiltonian for the lossless system in the rotating-wave approximation is given by

$$\hat{H}=\hbar\omega_0\hat{\mathcal{N}}+i\hbar g\hat{\mathcal{A}}, \tag{1}$$

where

$$\hat{\mathcal{N}}=(\hat{a}^\dagger\hat{a}+1/2)+\hat{\sigma}_3 \tag{2}$$

is the ‘‘excitation number’’ operator and

$$\hat{\mathcal{A}}=\hat{a}^\dagger\hat{\sigma}_- - \hat{a}\hat{\sigma}_+ = -\hat{\mathcal{A}}^\dagger \tag{3}$$

is an anti-Hermitian ‘‘excitation exchange operator’’; ω_0 is the atomic transition frequency and cavity resonance frequency, and g is the dipole coupling constant.

The Hilbert space for the atom and cavity mode is

$$\mathcal{H}=\mathcal{H}_{\mathrm{atom}}\otimes\mathcal{H}_{\mathrm{cav}}. \tag{4}$$

The ground and excited states of the atom are denoted $|g\rangle$ and $|e\rangle$, and the Fock number states, $\{|N\rangle\}$, are the energy eigenstates for the quantized electromagnetic field. Together these states form a basis which diagonalizes the excitation number operator $\hat{\mathcal{N}}$. The spectroscopy of the Jaynes-Cummings system follows from the eigenstates of the total Hamiltonian, the so-called dressed states which diagonalize both $\hat{\mathcal{N}}$ and $\hat{\mathcal{A}}$. In the dressed-state basis there is the ground state

$$|0)\equiv|0\rangle|g\rangle \tag{5}$$

with energy $E_0=0$, and excited-state couplets

$$|N)_\pm\equiv 2^{-1/2}(|N-1\rangle|+\rangle\pm i|N\rangle|g\rangle), \quad N>0 \tag{6}$$

which satisfy the eigenvalue equation

$$\hat{H}|N)_\pm=\hbar(N\omega_0\pm\sqrt{N}g)|N)_\pm . \tag{7}$$

The dressed states entangle the degrees of freedom of the atom and the electromagnetic field, formalizing the picture of the Jaynes-Cummings system as a single, composite entity. The defining characteristic of the Jaynes-Cummings energy spectrum is the splitting, $2\hbar\sqrt{N}g$, of the excited-state couplets. Our interest is with the transitions between the first and second excited states. The goal is to observe the four absorption resonances at frequencies $\omega_0+(\sqrt{2}\pm1)g$ and $\omega_0-(\sqrt{2}\pm1)g$.

B. Difficulties with atomic beams

Transitions between the first and second excited states can be accessed in two-photon absorption. Experiments with atomic beams face two difficulties, however. First, the energy spectrum to be measured is specifically the spectrum of *one* atom coupled to the electromagnetic field. On the other hand, the number of atoms produced in a given interaction volume by an atomic-beam will fluctuate in time. Of course, the solution to this is in principle straightforward: For a sufficiently low atomic-beam density the fluctuations are predominantly between zero atoms—most of the time—and one atom—on occasions. A measurement which detects the atoms, as in the recent microwave experiments [11,12,25], then records only one-atom events. The same strategy can work for optical frequencies where photons are detected in place of the atoms; one may illuminate the interaction volume with a probe laser off the cavity axis so that on-axis detection records no photons unless an atom is present.

A question remains, however, as to what is a sufficiently low atomic-beam density. This question is nontrivial for optical cavities, where the interaction volume is not bounded in the plane transverse to the cavity axis. We discuss the question elsewhere [23] and simply summarize our answer here. It is based on a consideration of the probability distribution of collective (multiatom) coupling strengths calculated from an ensemble of the spatial configurations of atoms realized in an atomic beam. In the limit of low atomic-beam density, the shape of this probability distribution, for coupling strengths not too close to zero, approaches an asymptotic form—the form obtained for one atom uniformly distributed in space. We therefore identify one-atom conditions with the requirement that the defined probability distribution closely approach this asymptotic form. The conditions are ensured if the average number of atoms within the Gaussian mode waist is much less than unity. In what follows we assume this is so and derive all results for strictly one-atom interactions.

There is a second difficulty, which at optical frequencies is not solved by using a low atomic-beam density but in fact becomes worse. The problem is the variation of the dipole coupling constant with the location of the atom in the cavity mode. For a standing-wave TEM$_{00}$ mode,

$$g(\boldsymbol{r})=g_{\max}\cos(kz)e^{-r^2/w_0^2}, \tag{8}$$

with $k=2\pi/\lambda$, where k is the wave number, λ the wavelength, and w_0 is the mode waist. $g_{\max}$ is the dipole coupling constant when the atom is located on the cavity axis at an antinode of the standing wave. Only rarely, however, will the atom even come close to this location. More realistically, the ensemble of single atoms produced by an atomic beam will be uniformly distributed in space. The corresponding probability distribution of dipole coupling constants is derived in the Appendix:

$$P(g)=V_F^{-1}\frac{\cos^{-1}(g/g_{\max})}{g}, \quad Fg_{\max}\leq g\leq g_{\max}, \tag{9}$$

where V_F, $0<F<1$, is a finite interaction volume introduced for normalization. The distribution is monotonically decreasing, and small values of the dipole coupling constant are by far the most probable; indeed the probability distribution diverges as g (and F) approaches zero. (With the restriction to one atom, the limit $F\rightarrow0$ corresponds to a zero beam density.)

At microwave frequencies this spatial dependence of g is not a major source of difficulty [11,12,25]. Even for an open standing-wave cavity [12], the atoms can be confined to intersect the mode axis at an antinode, with very small dispersion relative to the Gaussian waist and the period of the standing wave. Also, since there is no photon loss during the atom's transit time, along its trajectory the changing dipole coupling constant may simply be integrated in time. At optical frequencies, the situation is quite different. Transverse confinement of the atomic beam on the scale of the wavelength might be achieved using atom-optics techniques but is certainly very difficult. Even more important is the consequence of photon loss during the transit time of the atom. This changes the physics completely. At optical frequencies, measurements are made in the frequency domain, by detecting photons scattered *while* the atom and cavity mode interact [13–15]. Under these conditions $P(g)$ represents an ensemble of different Jaynes-Cummings systems, a source of inhomogeneous broadening. More precisely, only for atoms placed as stationary objects in the cavity mode is this interpretation exact. It is a reasonable one, however, for sufficiently slowly moving atoms, atoms whose velocity, v, satisfies the inequality [23]

$$\frac{v/w_0}{\frac{1}{2}(\kappa+\gamma_I/2)}<\left(\frac{e}{2}\right)^{1/2}\frac{\frac{1}{2}(\kappa+\gamma_I/2)}{g_{\max}}, \tag{10}$$

where $\frac{1}{2}(\kappa+\gamma_I/2)$ is the half-width of the first excited state; κ is the half-width of the cavity and $\gamma_I/2$ is the cavity-inhibited half-width of the atom. In this paper we take the atom, at each point along its trajectory, to be at rest. We have shown that calculations based on this assumption are in good agreement with quantum trajectory simulations for moving atoms [23].

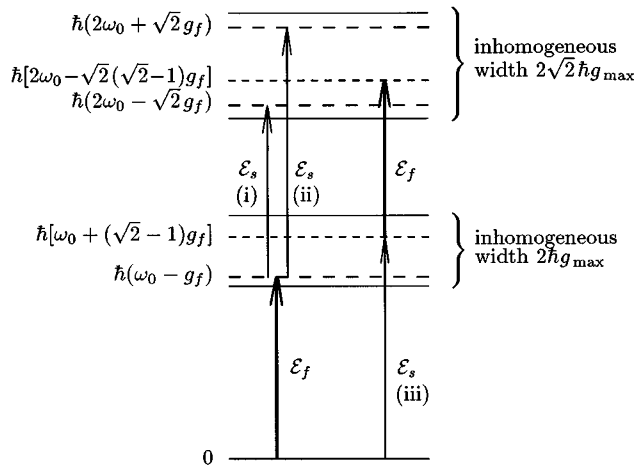

FIG. 1. Selection of two subpopulations within the dipole coupling constant distribution in two-photon absorption. The ground-state energy and the inhomogeneously broadened energy bands associated with the first and second couplet of the Jaynes-Cummings spectrum are shown. The absorption paths on the left select the coupling strength $g=g_f$ and the path on the right selects $g=(\sqrt{2}-1)g_f$. The labels (i), (ii), and (iii) identify corresponding two-photon resonances in Figs. 1, 3, 4, and 8.

C. Two-photon excitation

The goal now is to detect homogeneously broadened absorption resonances between the first and second Jaynes-Cummings couplets in the presence of the inhomogeneous broadening $P(g)$. Our strategy is a standard one taken from sub-Doppler spectroscopy; a subensemble of Jaynes-Cummings systems is selected within the inhomogeneous line. The selection is done in two-photon absorption with excitation by a bichromatic field,

$$\mathcal{E}(t)=\mathcal{E}_f e^{-i\omega_f t}+\mathcal{E}_s e^{-i\omega_s t}, \tag{11}$$

coupled to the atom. ω_f is a fixed frequency and the spectrum is taken as ω_s is scanned. We may assume $\mathcal{E}_f$ is real, without loss of generality, if a random relative phase is carried by the complex amplitude $\mathcal{E}_s$. The phase accounts for the random initiation time of the interaction with the atom. Actually, nothing would be lost if $\mathcal{E}_s$ were also taken to be real since the cycle-averaged (over the beat period $2\pi/|\omega_f-\omega_s|$) two-photon excitation is independent of this phase. The amplitudes of the two chromatic components must be large enough to produce a population in the second excited states, but not so large that significant Stark shifts or occupation of the higher-order excited states occurs.

The two-photon transitions shown on the left in Fig. 1 illustrate the basic selection process. If the atom is located at $\mathbf{r}$ such that

$$g(\mathbf{r})=g_f,\quad g_f\equiv|\omega_f-\omega_0|, \tag{12}$$

one of the ground to first excited-state transitions of the Jaynes-Cummings system is resonant with ω_f. Then two two-photon resonances occur as ω_s is scanned: with $\omega_f=\omega_0-g_f$, as illustrated, the first to second excited-state resonances are at $\omega_s=\omega_0-(\sqrt{2}-1)g_f$ and $\omega_s=\omega_0+(\sqrt{2}+1)g_f$; with $\omega_f=\omega_0+g_f$ the resonances are at $\omega_s=\omega_0+(\sqrt{2}-1)g_f$ and $\omega_s=\omega_0-(\sqrt{2}+1)g_f$.

If $\mathcal{E}_f \gg \mathcal{E}_s$, as in a normal pump-probe configuration, these would be the only two-photon resonances to consider for fixed ω_f. This relation between amplitudes is found to be unsatisfactory, however, due to the nonresonant two-photon absorption background produced by $\mathcal{E}_f$. In order to reduce this background, it is actually preferable for $\mathcal{E}_f$ to be equal to, or even somewhat smaller than, $\mathcal{E}_s$. Then the two-photon resonance shown on the right in Fig. 1 is also significant. In this case ω_f selects the resonance frequency of the second absorbed photon, and two-photon resonance is possible when

$$g(\mathbf{r})=(\sqrt{2}-1)g_f. \tag{13}$$

As ω_s is scanned, the two-photon resonance occurs for $\omega_s=\omega_0+(\sqrt{2}-1)g_f$, as illustrated, when $\omega_f=\omega_0-g_f$, and for $\omega_s=\omega_0-(\sqrt{2}-1)g_f$ when $\omega_f=\omega_0+g_f$.

In summary, the bichromatic field (11) selects two subpopulations from the inhomogeneous distribution $P(g)$, subpopulations whose dipole coupling constants are close to the values given by Eqs. (12) and (13). One subpopulation undergoes two two-photon resonances in absorption as ω_s is scanned, and the other, one two-photon resonance. The relative sizes of the two subpopulations change with changes in $P(g)$. In the following we consider the distribution (9), and, in addition, a distribution for an atomic beam which confines the atoms to the vicinity of the antinodes and the cavity axis. The analytical expression for the second distribution is quite complicated and therefore stated only in the Appendix.

D. Photon coincidence detection

Once the system reaches the second excited state it will eventually relax to the ground state, emitting two photons, separated in time by something on the order of the first excited-state lifetime. The couplet at the second excited state comprises two entangled states,

$$|2\rangle_{\pm}\equiv 2^{-1/2}(|1\rangle|e\rangle\pm i|2\rangle|g\rangle), \tag{14}$$

both of which can relax by one of two decay channels: either two photons are emitted through the cavity mirrors, $|2\rangle_{\pm}\rightarrow\hat{a}^2|2\rangle_{\pm}=\pm i\sqrt{2}|0\rangle$, or one photon is emitted through the mirrors and one out the sides of the cavity, $|2\rangle_{\pm}\rightarrow\hat{a}\hat{\sigma}_-|2\rangle_{\pm}=\pm i|0\rangle$. We consider detection of the photons emitted through the cavity mirrors. This decay channel is favored by both a higher collection efficiency and a larger transition matrix element.

As ω_s is scanned, the flux of photons emitted through the cavity mirrors should increase at each two-photon absorption resonance. There is a much larger contribution to the photon flux from one-photon scattering, however—i.e., scattering by the subpopulations with

$$g(\mathbf{r})\approx|\omega_f-\omega_0|\quad\text{or}\quad g(\mathbf{r})\approx|\omega_s-\omega_0|, \tag{15}$$

the subpopulations in resonance with ω_f or ω_s. In general, the two-photon scattering and one-photon scattering are not separated in frequency space, and it is necessary to separate them by some other means. We propose to use photon statistics. It is from this that the name *photon correlation spectroscopy* is derived.

The basic idea is one common in particle physics—to identify an unstable state by correlating its decay products. In the present case, the products are a photon pair; two-photon decay will produce an identifiable photon pair—a pair resolved in time from the one-photon background—when the on-resonance one-photon flux [Eq. (15)] is much less than the inverse lifetime of the intermediate states. This leads to the requirement

$$|\mathcal{E}_{f,s}|^2/(\kappa+\gamma_I/2)^2 \ll 1. \tag{16}$$

For such weak excitation we propose to measure the photon coincidence rate as a function of ω_s. At each two-photon absorption resonance the rate will increase. Of course, coincidence must be defined in practice by a time window, τ_w, on the order of the lifetime of the cavity decay channel κ^{-1}. The narrower the window, the better the selection against chance coincidences of two one-photon events. The spectrum measured in this way is given by the second-order correlation function, $g^{(2)}_{\omega_f}(\omega_s,\tau)$, integrated with respect to τ over the window τ_w. In this paper we assume $\kappa\tau_w \ll 1$ and simply calculate $g^{(2)}_{\omega_f}(\omega_s,0)$, or more specifically the probability to find two photons in the cavity, $\langle \hat{a}^{\dagger 2}\hat{a}^2\rangle_{\omega_f}(\omega_s)$. Good agreement is obtained with quantum trajectory simulations using a finite coincidence window [23].

E. Subtracting background counts

The aim is to measure the unequal splittings of the first and second excited-state couplets. Just because the splittings are unequal, exact resonance on both the $|0)\rightarrow|1)_\pm$ and $|1)_\pm\rightarrow|2)_\pm$ transitions can only be achieved by absorbing one photon of frequency ω_f and one of frequency ω_s. Two types of nonresonant two-photon absorption can occur, however, absorption in which both photons have frequency ω_f or both have frequency ω_s. First, nonresonant two-photon absorption will occur for the subpopulations satisfying Eq. (15)—i.e., when the transition $|0)\rightarrow|1)_\pm$, but not $|1)_\pm\rightarrow|2)_\pm$, is on resonance. This provides a two-photon background driven by both $\mathcal{E}_f$ and $\mathcal{E}_s$. The second possibility is for exact two-photon resonance, but without resonance on the $|0)\rightarrow|1)_\pm$ transition. If ω_f is set very close to $\omega_0\pm g_{\max}$, as illustrated in Fig. 1, exact resonance is not possible for two photons of frequency ω_f. It is possible on the other hand for two photons of frequency ω_s, and this provides a second contribution to the two-photon background driven by $\mathcal{E}_s$.

The most damaging background is that driven by $\mathcal{E}_s$, since as ω_s is scanned, this maps out $P(g)$, and hence acquires the $2g_{\max}$ inhomogeneous width. Given the divergence of $P(g)$ as $g\rightarrow 0$, there is a good possibility for swamping the selected two-photon resonances. Such is the case, at least, for two of the selected resonances. For the third—at $\omega_s=\omega_0+(\sqrt{2}+1)g_f$ in Fig. 1—the resonance frequency lies outside the inhomogeneous line and the resonance should be resolved even in the presence of the two-photon background.

Actually, in all cases the situation is less gloomy than it might appear, since one can subtract the two-photon background driven by $\mathcal{E}_s$. To do so a second measurement of the photon coincidence rate is made with $\mathcal{E}_f=0$ and subtracted from the first. This difference is the *photon coincidence spectrum*, the final result of the proposed technique. Of course, the two-photon background driven by $\mathcal{E}_f$ remains. It may be minimized, however, by decreasing $\mathcal{E}_f$ relative to $\mathcal{E}_s$ while keeping their product constant.

We have calculated the photon coincidence spectrum, the difference

$$\Delta^{(2)}(\omega_s) \equiv \langle \hat{a}^{\dagger 2}\hat{a}^2\rangle_{\omega_f}(\omega_s) - \langle \hat{a}^{\dagger 2}\hat{a}^2\rangle(\omega_s)|_{\mathcal{E}_f=0}, \tag{17}$$

using the assumptions and approximations described above. The first step of the calculation is to solve the master equation for the Jaynes-Cummings system with radiative damping under the bichromatic excitation specified by Eq. (11).

III. SOLVING THE MASTER EQUATION

Including cavity damping, at the rate 2κ, radiation into free space from the atom, at the rate γ_I, and driving of the atom by the classical field $\mathcal{E}(t)$, the master equation for the Jaynes-Cummings system density matrix ρ is given by

$$\begin{aligned}\dot{\rho} = {} & [\hat{H},\rho]/i\hbar + [\mathcal{E}(t)\hat{\sigma}_+ - \mathcal{E}^*(t)\hat{\sigma}_-,\rho] \\ & + (\gamma_I/2)(2\hat{\sigma}_-\rho\hat{\sigma}_+ - \hat{\sigma}_+\hat{\sigma}_-\rho - \rho\hat{\sigma}_+\hat{\sigma}_-) \\ & + \kappa(2\hat{a}\rho\hat{a}^\dagger - \hat{a}^\dagger\hat{a}\rho - \rho\hat{a}^\dagger\hat{a}),\end{aligned} \tag{18}$$

where $\hat{H}$ is the Jaynes-Cummings Hamiltonian, Eq. (1). We solve the master equation in the dressed-state basis, designating the density-matrix elements as

$$\begin{gathered}(\rho)_{00} \equiv (0|\rho|0), \quad (\rho)^{\pm}_{0N} \equiv (0|\rho|N)_\pm, \\ (\rho)^{\epsilon'\epsilon}_{N'N} \equiv {}_{\epsilon'}(N'|\rho|N)_\epsilon, \quad \epsilon',\epsilon \in \{\pm\}.\end{gathered} \tag{19}$$

Provided that excitation to higher energies is negligible, the representation may be truncated beyond the Jth couplet. The truncation can be justified, for any J, by requiring the amplitudes $\mathcal{E}_f$ and $\mathcal{E}_s$ to be sufficiently small. Since our interest is with transitions from the first to the second couplet, the lowest useful truncation is at $J=2$. The formalism developed in this section holds for any J, but when applying it in explicit calculations we have taken $J=3$. In this case, Eq. (18) constitutes a coupled set of linear equations for 49 matrix elements.

We wish to find the asymptotic solution to Eq. (18), $\lim_{t\rightarrow\infty}\rho(t)$. Due to the bichromatic excitation, this is not a stationary state. The explicit time dependence at frequency ω_f can be removed by working in an interaction picture, taking the free Hamiltonian as $\hat{H}_0=\hbar\omega_f\hat{N}$. We then write

$$\mathcal{E}(t)=\mathcal{E}_f+\mathcal{E}_s e^{-i\delta t}, \quad \delta\equiv\omega_s-\omega_f, \tag{20}$$

and the frequency ω_0 in the Hamiltonian [Eq. (1)] is replaced by $\omega_0-\omega_f$. An explicit time dependence at frequency δ still, however, remains. As a consequence, the asymptotic

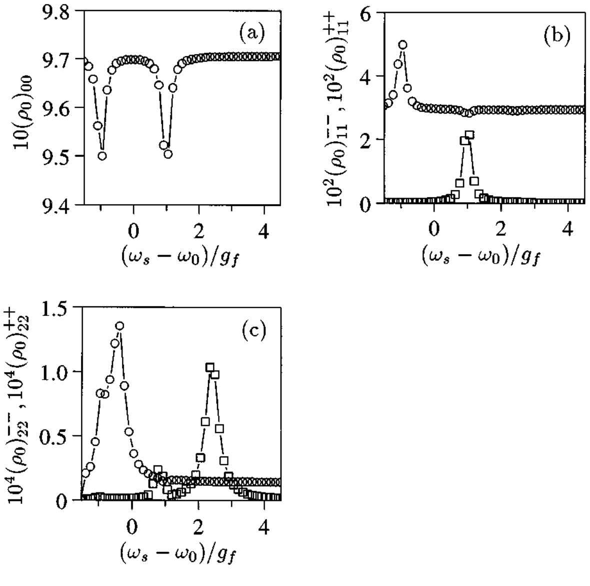

FIG. 2. Diagonal density-matrix elements plotted as a function of ω_s/g_f for $\gamma_I/2\kappa=1$, $g_f/\kappa=g/\kappa=9$ and $\mathcal{E}_f/\kappa=\mathcal{E}_s/\kappa=0.25$: (a) $(\rho_0)_{00}$, (b) $(\rho_0)_{11}^{--}$ (circles) and $(\rho_0)_{11}^{++}$ (boxes), and (c) $(\rho_0)_{22}^{--}$ (circles) and $(\rho_0)_{22}^{++}$ (boxes).

solution executes a steady oscillation with period $2\pi/\delta$. We therefore solve Eq. (18) in the Bloch function approach. We adopt the series expansion

$$\rho(t)=\sum_{k=-\infty}^{\infty}\rho_k(t)e^{-ik\delta t}, \tag{21}$$

where the asymptotic solution satisfies

$$\lim_{t\to\infty}\dot{\rho}_k(t)=0. \tag{22}$$

Then

$$\dot{\rho}(t)=\sum_{k=-\infty}^{\infty}[\dot{\rho}_k(t)-ik\delta\rho_k(t)]e^{-ik\delta t} \tag{23}$$

and

$$\lim_{t\to\infty}\dot{\rho}(t)=-i\delta\sum_{k=-\infty}^{\infty}k\rho_k(t)e^{-ik\delta t}. \tag{24}$$

Substituting the expansions (21) and (24) into the master equation replaces the differential equation (18) by a tridiagonal recurrence relation connecting the time-independent operators ρ_k.

The $(2J+1)\times(2J+1)$ independent complex components of the density operator in the dressed-state basis can be replaced by a complex vector $\boldsymbol{y}$ of length $(2J+1)\times(2J+1)$. Similarly, the operator ρ_k is replaced by the vector $\boldsymbol{y}_k$. The latter can be constructed such that

$$\boldsymbol{y}_k=(\boldsymbol{y}_{-k})^*, \tag{25}$$

which guarantees that $\boldsymbol{y}_0$, the dc component of the asymptotic solution, is real. Our ultimate concern is with this dc component, since it is from this that the time-averaged expectations which determine the photon coincidence spectrum are to be calculated. We must, nevertheless, develop a full solution scheme for the tridiagonal recurrence relation, even to obtain this one density operator component. In the new notation, the asymptotic form of the master equation is

$$\mathcal{E}_s\boldsymbol{P}\boldsymbol{y}_{k-1}+(ik\delta+\boldsymbol{Q})\boldsymbol{y}_k+\mathcal{E}_s\boldsymbol{R}\boldsymbol{y}_{k+1}=\boldsymbol{0}, \tag{26}$$

where $\boldsymbol{P}$ and $\boldsymbol{R}$ are complex matrices of dimension $(2J+1)\times(2J+1)$, and $\boldsymbol{Q}$ is a real $(2J+1)\times(2J+1)$ matrix. Setting $k=0$ in this expression and using the identity (25) with $k=1$, we see that the matrices $\boldsymbol{P}$ and $\boldsymbol{R}$ are necessarily related by

$$\mathcal{E}_s\boldsymbol{P}=(\mathcal{E}_s\boldsymbol{R})^* \tag{27}$$

and

$$\boldsymbol{Q}\boldsymbol{y}_0+2\mathrm{Re}(\mathcal{E}_s\boldsymbol{R}\boldsymbol{y}_1)=\boldsymbol{0}. \tag{28}$$

In order to solve the recurrence relation (26) we introduce a set of transformation matrices $\{\boldsymbol{S}_k\}$ [26,27] such that

$$\boldsymbol{y}_{k+1}=\boldsymbol{S}_{k+1}\boldsymbol{y}_k. \tag{29}$$

The $\boldsymbol{S}_k$ are not necessarily invertible, but they allow us to rewrite the recurrence relation in the form

$$\mathcal{E}_s^*\boldsymbol{R}^*\boldsymbol{y}_{k-1}=-(ik\delta+\boldsymbol{Q}+\mathcal{E}_s\boldsymbol{R}\boldsymbol{S}_{k+1})\boldsymbol{y}_k, \tag{30}$$

producing the result

$$\boldsymbol{S}_k\boldsymbol{y}_{k-1}=\boldsymbol{y}_k=-\mathcal{E}_s^*(ik\delta+\boldsymbol{Q}+\mathcal{E}_s\boldsymbol{R}\boldsymbol{S}_{k+1})^{-1}\boldsymbol{R}^*\boldsymbol{y}_{k-1}, \tag{31}$$

where the first equality follows with a further application of the identity (29). As $\boldsymbol{y}_k$ (hence $\boldsymbol{y}_{k-1}$) is chosen arbitrarily, the recurrence relation

$$\boldsymbol{S}_k=-\mathcal{E}_s^*(ik\delta+\boldsymbol{Q}+\mathcal{E}_s\boldsymbol{R}\boldsymbol{S}_{k+1})^{-1}\boldsymbol{R}^* \tag{32}$$

is thus established. Equation (28) now appears as

$$[\boldsymbol{Q}+2\mathrm{Re}(\mathcal{E}_s\boldsymbol{R}\boldsymbol{S}_1)]\boldsymbol{y}_0=\boldsymbol{0}; \tag{33}$$

hence, $\boldsymbol{y}_0$, the dc component of the asymptotic density operator, is the eigenvector with zero eigenvalue of the matrix

$$\boldsymbol{M}\equiv\boldsymbol{Q}+2\mathrm{Re}(\mathcal{E}_s\boldsymbol{R}\boldsymbol{S}_1). \tag{34}$$

The program is to solve the recurrence relation (32) for $\boldsymbol{S}_1$ and compute the zero eigenvector of $\boldsymbol{M}$. The first step is accomplished using a continued fraction expansion, which for sufficiently small $\mathcal{E}_s$ may be terminated at first order. Then

$$\boldsymbol{S}_1\approx-\mathcal{E}_s^*[i\delta+\boldsymbol{Q}-|\mathcal{E}_s|^2\boldsymbol{R}(2i\delta+\boldsymbol{Q})^{-1}\boldsymbol{R}^*]^{-1}\boldsymbol{R}^*, \tag{35}$$

and, hence,

$$\boldsymbol{M}\approx\boldsymbol{Q}-2|\mathcal{E}_s|^2\mathrm{Re}\{\boldsymbol{R}[i\delta+\boldsymbol{Q}-|\mathcal{E}_s|^2\boldsymbol{R}(2i\delta+\boldsymbol{Q})^{-1}\boldsymbol{R}^*]^{-1}\boldsymbol{R}^*\}. \tag{36}$$

Note that $\boldsymbol{M}$, and therefore $\boldsymbol{y}_0$, is independent of the relative phase (contained in $\mathcal{E}_s$) of $\mathcal{E}_f$ and $\mathcal{E}_s$.

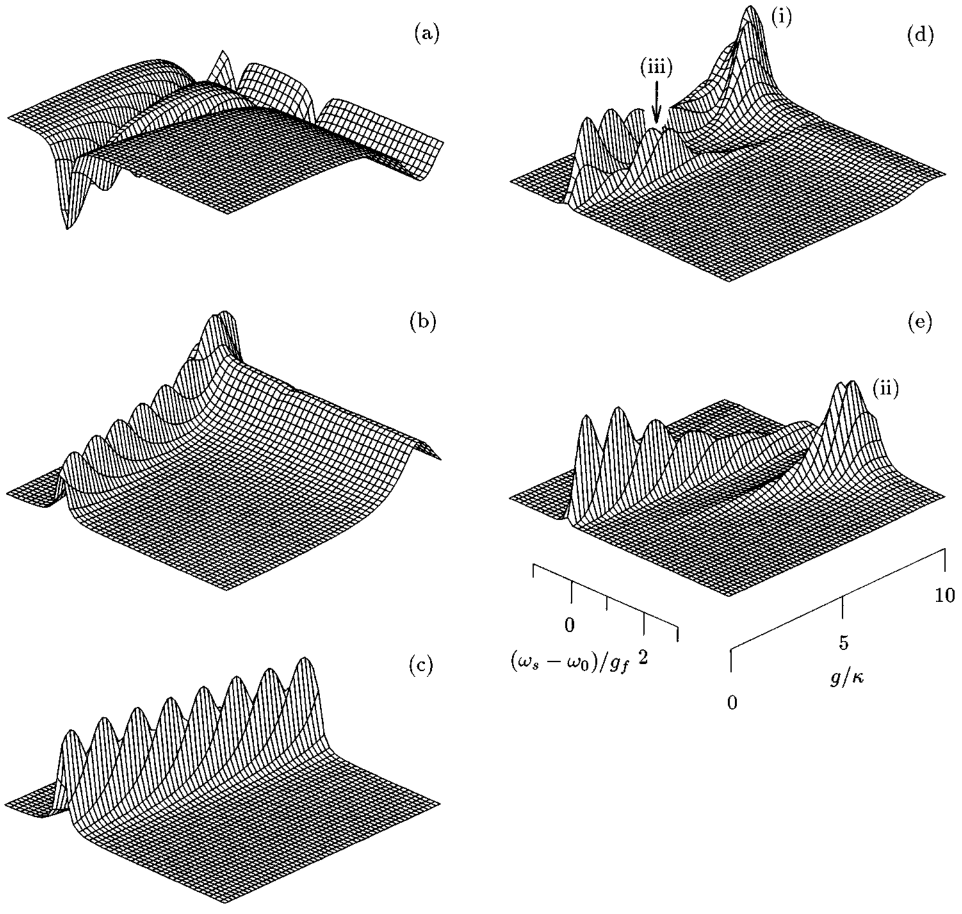

FIG. 3. Diagonal density-matrix elements plotted as a function of g/κ and ω_s/g_f for $\gamma_I/2\kappa=1$, $g_f/\kappa=9$, and $\mathcal{E}_f/\kappa=\mathcal{E}_s/\kappa=0.25$: (a) $(\rho_0)_{00}$, (b) $(\rho_0)_{11}^{--}$, (c) $(\rho_0)_{11}^{++}$, (d) $(\rho_0)_{22}^{--}$, and (e) $(\rho_0)_{22}^{++}$. Only the functional dependence is shown; the scales of the plots can be read from Fig. 2. The labels (i), (ii), and (iii) identify corresponding two-photon resonances in Figs. 1, 3, 4, and 8.

IV. RESULTS AND DISCUSSION

We are now in a position to calculate the photon correlation spectrum. The calculation is done numerically. First, the asymptotic solution for the density matrix, ρ_0, is found, as the zero eigenvector of the matrix (36), and from this $\Delta^{(2)}(\omega_s)$ is calculated for fixed g [Eq. (17)]. Finally, the average is taken over the inhomogeneous broadening $P(g)$. In this section we discuss the results. We begin with results for the matrix elements of ρ_0 before taking the average over $P(g)$. All calculations are based on the parameters $g_{\max}/\kappa=2g_{\max}/\gamma_I=10$, which should be compared with the best experimental values, $g_{\max}/\kappa=12$, $2g_{\max}/\gamma_I=2.9$, reported for the optical frequency domain [28]. Our choice of parameters is optimistic but not an unreasonable goal for future experiments.

A. Homogeneous broadening

The ideal experiment would be conducted without inhomogeneous broadening and with ω_f tuned to one of the ground to first excited-state transitions. Then $P(g)=\delta(g-g_f)$, and only two of the three two-photon absorption resonances mentioned in Sec. II C exist; for example, with $\omega_f=\omega_0-g_f$, the pair shown on the left in Fig. 1. For these conditions, we plot the occupation probabilities of the first five dressed states as a function of ω_s in Fig. 2. $(\rho_0)_{00}$ and $(\rho_0)_{11}^{--}$ exhibit background occupation probabilities determined by the fixed, resonant excitation of the $|0\rangle\rightarrow|1\rangle_-$ transition. The expected backgrounds are readily calculated from a two-state approximation [29]

$$(\rho_0)_{11}^{--}\approx\frac{\mathcal{E}_f^2}{\frac{1}{2}(\kappa+\gamma_I/2)^2+2\mathcal{E}_f^2}=\frac{1}{34},$$

(37)

$$(\rho_0)_{00}\approx 1-(\rho_0)_{11}^{--},$$

in agreement with the values observed in the figure. Two dips appear against the background in the ground-state occupation probability, evidence of the one-photon absorption resonances at $\omega_s=\omega_0\pm g_f$, and corresponding peaks appear in the occupation probabilities of the first excited states. Note also the small reduction in the occupation probability of state $|1\rangle_-$ when resonant absorption occurs to state $|1\rangle_+$. This is a saturation effect due to competition between the absorption on the $|0\rangle\rightarrow|1\rangle_-$ and $|0\rangle\rightarrow|1\rangle_+$ transitions. In the presence of inhomogeneous broadening the feature produces a Lamb dip, as shown in Sec. IV B.

Figure 2(c) shows the occupation probabilities for the second couplet. $(\rho_0)_{22}^{--}$ exhibits the two-photon background driven by $\mathcal{E}_f$. If the absorption resonance at frequency ω_f were harmonic, this background would follow from a Poisson distribution, the excitation distribution for a coherent state. The two-photon and one-photon backgrounds would then be related, with $(\rho_0)_{22}^{--}=\frac{1}{2}[(\rho_0)_{11}^{--}]^2\approx 4.5\times 10^{-4}$. The two-photon background is actually smaller by approximately thirty times. The reduction is due to two differences between the driven Jaynes-Cummings system (‘‘vacuum’’ Rabi resonance) and a driven harmonic resonance [29]. The ratio of transition matrix elements for the $|0\rangle\rightarrow|1\rangle_-$ and

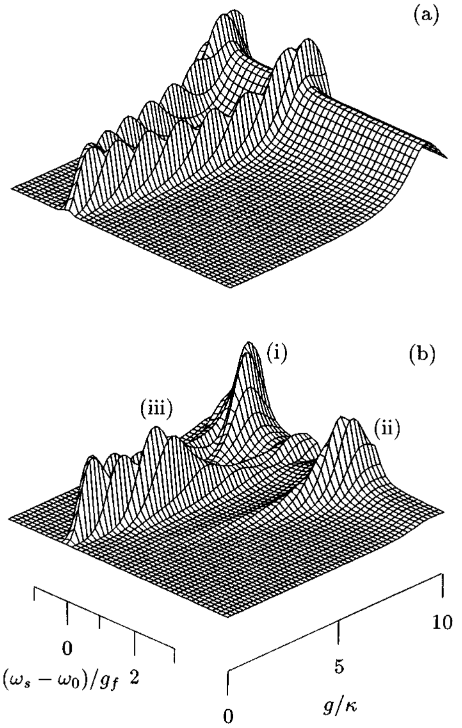

FIG. 4. (a) $\langle a^\dagger a\rangle_{\omega_f}(\omega_s)$ and (b) $\langle a^{\dagger 2}a^2\rangle_{\omega_f}(\omega_s)$ plotted as a function of g/κ for $\gamma_I/2\kappa=1$, $g_f/\kappa=9$, and $\mathcal{E}_f/\kappa=\mathcal{E}_s/\kappa=0.25$. Only the functional dependence is shown; the scales of the plots can be read from Figs. 2(b) and 2(c). The labels (i), (ii), and (iii) identify corresponding two-photon resonances in Figs. 1, 3, 4, and 8.

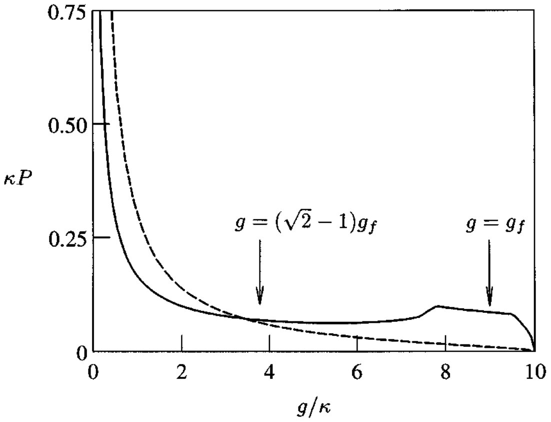

FIG. 5. Dipole coupling constant distributions for $g_{\max}/\kappa=10$ and $F=0.01$. The dashed curve is obtained without a (y,z)-plane mask [Eqs. (A4), (A8), and (A9)] and the solid curve with the mask $kz_{\max}=0.1\pi$, $y_{\max}/w_0=0.5$, as illustrated in Fig. 9 [Eqs. (A4), (A21), and (A8) (Range I), (A13) (Range II), (A17) (Range III), and (A20) (Range IV)]. The locations of the two subpopulations selected by ω_f [Eqs. (12) and (13)] are shown for $g_f=0.9g_{\max}$.

$|1)_-\rightarrow|2)_-$ transitions is different, and while ω_f is resonant with the first transition it is not resonant with the second. The second feature is, of course, what we aim to detect.

Against the two-photon background in $(\rho_0)_{22}^{--}$, the anticipated resonance at $\omega_s=\omega_0-(\sqrt{2}-1)g_f$ appears. The second two-photon resonance, at $\omega_s=\omega_0+(\sqrt{2}+1)g_f$, appears in $(\rho_0)_{22}^{++}$, and there is no significant background in this case.

It was noted in Sec. II E that when inhomogeneous broadening is present, the more important two-photon background is that driven by $\mathcal{E}_s$. One contribution to this background is from two-photon resonance in the absence of resonance on the $|0)\rightarrow|1)_\pm$ transition. This background is discernible in Fig. 2(c) as the two smaller resonances at $\omega_s=\omega_0+g_f/\sqrt{2}$ and $\omega_s=\omega_0-g_f/\sqrt{2}$. In the latter case the background resonance interferes with the much larger two-photon resonance at $\omega_s=\omega_0-(\sqrt{2}-1)g_f$.

In order to understand the effect of inhomogeneous broadening, which averages all these features for systems with different coupling constants, it helps to study the homogeneously broadened results for $g\equiv g(\mathbf{r})\neq g_f$. Figure 3 shows how the occupation probabilities for the first five dressed states change as a function of both ω_s and g. The curves of Fig. 2 are recovered from these three-dimensional plots by taking a cut along $g/\kappa=g_f/\kappa=9$. Figures 3(a), 3(b), and 3(c) show the splitting of the $|0)\rightarrow|1)_-$ and $|0)\rightarrow|1)_+$ one-photon resonances with increasing g; the resonances are mapped out as ω_s is scanned. In Figs. 3(a) and 3(b) the one-photon resonance with ω_f also appears, mapped out in this case as a function of g. The peak of the resonance at $g=g_f$ sets the one-photon background illustrated by Fig. 2(b). Note again the small saturation dip in this background, which will be recalled shortly as the source of a Lamb dip.

Figures 3(d) and 3(e) exhibit a total of six two-photon resonances. The three resonances selected by the transitions in Fig. 1 are indicated on the figures. Each of these is localized with respect to both ω_s and g. Two more resonances appear, as ω_s is scanned, for every value of g. These are the two-photon resonances which produce the background driven by $\mathcal{E}_s$. Finally, a small resonance appears in $(\rho_0)_{22}^{--}$, as a function of g, for fixed ω_s. This is the two-photon background driven by $\mathcal{E}_f$.

The measured quantities are the flux and rate of coincidences of photons emitted by the cavity, proportional, respectively, to $\langle\hat{a}^\dagger\hat{a}\rangle_{\omega_f}(\omega_s)$ and $\langle\hat{a}^{\dagger 2}\hat{a}^2\rangle_{\omega_f}(\omega_s)$. To a first approximation these quantities are given by the sums $[(\rho_0)_{11}^{--}+(\rho_0)_{11}^{++}]/2$ and $(\rho_0)_{22}^{--}+(\rho_0)_{22}^{++}$. The results displayed in Fig. 4 include the corrections to these expressions resulting from dressed-state coherences and higher excited states (in a seven-state basis). In Fig. 4(a) the saturation dip is now buried in the one-photon resonance. The two-photon resonances also interfere with one another to some extent, as can be seen in Fig. 4(b). The next step is to take the average, for each ω_s, over the inhomogeneous broadening $P(g)$; the obfuscation of detail will then be complete.

B. Inhomogeneous broadening

Two distributions of the dipole coupling constant are derived in the Appendix. The distribution given by Eq. (9) assumes a uniform distribution of the atom in space and a standing-wave TEM_{00} cavity mode. We also derive $P(g)$ under the assumption that a mask in the (y,z) plane (Fig. 9), transverse to the atomic beam, rejects atoms which do not pass close to the optic axis and an antinode of the standing wave [Eqs. (A4), (A21), and (A8) (Range I), (A13) (Range II), (A17) (Range III), and (A20) (Range IV)]. Equation (9) describes the inhomogeneous broadening in a worst-case

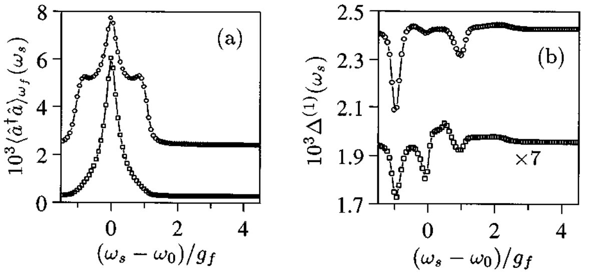

FIG. 6. $\langle a^\dagger a\rangle_{\omega_f}(\omega_s)$, averaged over the dipole coupling constant distribution, for $\gamma_l/2\kappa=1$, $g_f/\kappa=9$, $g_{\max}/\kappa=10$, and $\mathcal{E}_f/\kappa=\mathcal{E}_s/\kappa=0.25$: (a) before background subtraction, and (b) after background subtraction. The curves marked by boxes are obtained without a (y,z)-plane mask, and by circles with the mask $kz_{\max}=0.1\pi$, $y_{\max}/w_0=0.5$.

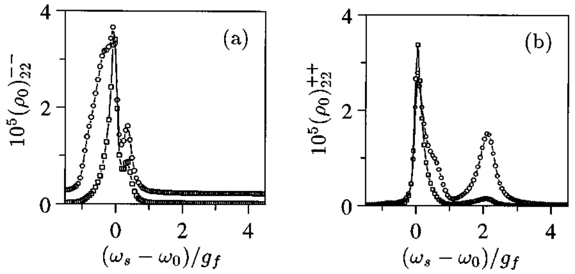

FIG. 7. Diagonal density-matrix elements for the second couplet, averaged over the dipole coupling constant distribution, plotted as a function of ω_s/g_f for $\gamma_l/2\kappa=1$, $g_f/\kappa=9$, $g_{\max}/\kappa=10$, and $\mathcal{E}_f/\kappa=\mathcal{E}_s/\kappa=0.25$: (a) $(\rho_0)_{22}^{--}$, and (b) $(\rho_0)_{22}^{++}$. The curves marked by boxes are obtained without a (y,z)-plane mask, and by circles with the mask $kz_{\max}=0.1\pi$, $y_{\max}/w_0=0.5$.

scenario. It is compared in Fig. 5 with the distribution produced by a strongly confining (y,z)-plane mask. The mask has little effect on the overall shape of the distribution; as there is no confinement along the atomic-beam axis, the dipole coupling constant is still distributed from 0 to $g_{\max}$ with a divergence at $g(\mathbf{r})=0$. The principal effect of the mask is to change the relative weights of the two subpopulations selected by ω_f. This, as will be seen, changes the relative heights of the peaks in the photon coincidence spectrum.

Figures 6–8 compare results for the two distributions plotted in Fig. 5. Clearly, the average against $P(g)$ obscures the resonances which are evident in Figs. 3 and 4. Figures 6(a) and 8(a) are the averages of Figs. 4(a) and 4(b), respectively, while Figs. 7(a) and 7(b) are the averages, respectively, of Figs. 3(d) and 3(e). Note first how the ''vacuum'' Rabi doublet of Fig. 4(a) is replaced in Fig. 6(a) by a single peak with the inhomogeneous width. The peak sits on the one-photon background driven by $\mathcal{E}_f$. The background is larger in the presence of the (y,z)-plane mask due to the increased weight, in this case, of the subpopulation selected with $g(\mathbf{r})=g_f$. The small saturation feature at $\omega_s=\omega_0+g_f$ seen in Figs. 2(b) and 3(b) is certainly not present. The Lamb dip produced by this feature appears, nevertheless, after subtracting the response obtained with $\mathcal{E}_f=0$. This is shown by the plots of the difference

$$\Delta^{(1)}(\omega_s)\equiv\langle\hat a^\dagger\hat a\rangle_{\omega_f}(\omega_s)-\langle\hat a^\dagger\hat a\rangle(\omega_s)|_{\mathcal{E}_f=0} \tag{38}$$

in Fig. 6(b). There are, in fact, two Lamb dips, one at $\omega_s=\omega_0+g_f$ and the other at $\omega_s=\omega_0-g_f$. These provide a measurement of the ''vacuum'' Rabi doublet under manifestly one-atom conditions. They appear both with and without the (y,z)-plane mask. The additional dip at $\omega_s=\omega_0$ in the latter case is due to the subtraction, which is sensitive to the heavy weighting by $P(g)$ of the response near $g(\mathbf{r})=0$.

Figure 6(b) also shows small features rising above the background. These are produced by two-photon absorption and provide an initial indication of the excited-state resonances identified in Fig. 1. Figures 7 and 8 show how these resonances are brought to prominence using photon coincidence detection. Even without background subtraction [Figs. 7 and 8(a)], the resonance at $\omega_s=\omega_0+(\sqrt{2}+1)g_f$ is clearly resolved while the resonances at $\omega_s=\omega_0\pm(\sqrt{2}-1)g_f$ are obscured by the two-photon background effects. After the subtraction [Eq. (17)] all three resonances are resolved, as shown in Fig. 8(b). They are well resolved both with and without the (y,z)-plane mask. Without the mask, however, the size of the central resonance is increased relative to the other two because of the increased weight of the subpopulation selected with $g(\mathbf{r})=(\sqrt{2}-1)g_f$ relative to that selected with $g(\mathbf{r})=g_f$.

Figure 8(b) is the central result of the paper. It is in good agreement with a quantum trajectory simulation of photon correlation spectroscopy [23]. The method used in its computation is numerically efficient and therefore suited for the optimization of future experiments.

V. CONCLUSIONS

The excited-state resonances of the Jaynes-Cummings system are notoriously difficult to observe. The difficulties are particularly acute at optical frequencies due to the small distance over which changes in the dipole coupling constant occur. Such changes inhomogeneously broaden the Jaynes-Cummings spectrum. *Photon correlation spectroscopy* makes the measurement of the first to second excited-state absorption resonances feasible for atoms prepared in a slowed, dilute atomic beam [23].

Here, a thorough analysis of the considerations motivating the idea of photon correlation spectroscopy has been given,

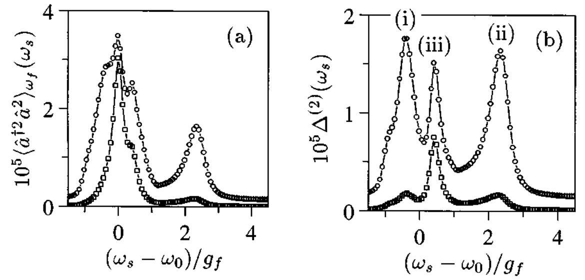

FIG. 8. $\langle a^{\dagger 2}a^2\rangle_{\omega_f}(\omega_s)$, averaged over the dipole coupling constant distribution, for $\gamma_l/2\kappa=1$, $g_f/\kappa=9$, $g_{\max}/\kappa=10$, and $\mathcal{E}_f/\kappa=\mathcal{E}_s/\kappa=0.25$: (a) before background subtraction, and (b) after background subtraction. The curves marked by boxes are obtained without a (y,z)-plane mask, and by circles with the mask $kz_{\max}=0.1\pi$, $y_{\max}/w_0=0.5$. The labels (i), (ii), and (iii) identify corresponding two-photon resonances in Figs. 1, 3, 4, and 8.

and an analytic theory for calculating the photon coincidence spectrum has been developed in the one-atom, quasistatic approximation. The master equation for the Jaynes-Cummings system driven by a bichromatic field was solved for a fixed dipole coupling constant in a lowest-order continued-fraction expansion. Inhomogeneous broadening was taken into account by an average over the distribution, $P(g)$, of the dipole coupling constant. An explicit expression for this distribution was derived for an atomic beam traversing a standing-wave TEM_{00} cavity mode.

Results for the one-photon and two-photon system response both before and after taking the average over the inhomogeneous broadening have been presented. These results clearly show the selection of excited-state resonances with definite g, in spite of strong two-photon background effects. In addition, the one-photon ‘‘vacuum’’ Rabi spectrum is present under manifestly one-atom conditions as a Lamb dip doublet. The prospects for future measurements of the Jaynes-Cummings spectrum at optical frequencies appear to be good.

ACKNOWLEDGMENTS

The work of H.J.C. is supported by the National Science Foundation under Grant No. PHY-9531218.

APPENDIX: DIPOLE COUPLING CONSTANT DISTRIBUTIONS

In this appendix we derive the two dipole coupling constant distributions used to account for inhomogeneous broadening in Sec. IV B. We consider an atomic beam which travels in the positive x direction and whose center intersects the optic axis (z axis) of a standing-wave TEM_{00} cavity mode at the coordinate origin $x=y=z=0$. An atom located at (x,y,z) couples to the cavity mode with dipole coupling constant

$$g(x,y,z)=g_{\max}\cos(kz)e^{-(x^2+y^2)/w_0^2}, \tag{A1}$$

$k=2\pi/\lambda$; k is the wave number, λ the wavelength, and w_0 the mode waist. $g_{\max}$ is the maximum possible value of the dipole coupling constant, realized for an atom located on the cavity axis at an antinode of the standing wave. For $g<g_{\max}$, $g(x,y,z)=g$ defines a string of disconnected closed surfaces on which the dipole coupling strength is constant; each surface encloses one antinode of the standing wave. For simplicity, we assume the atomic beam intersects exactly M (an odd integer) of these surfaces—i.e., the transverse profile of the atomic beam is confined to the range $-M\lambda/4\leq z\leq M\lambda/4$. We define $V(g)$ to be the interaction volume enclosed by $g(x,y,z)=g$:

$$V(g)\equiv\{(x,y,z):g(x,y,z)\geq g,|z|\leq M\lambda/4\}. \tag{A2}$$

Since very weakly coupled atoms have a negligible effect on the cavity field, it is convenient to introduce a cutoff in the dipole coupling constant. To this end we confine our attention to atoms located within the volume

$$V_F=V(Fg_{\max}), \quad F<1, \tag{A3}$$

for which $g(x,y,z)\geq Fg_{\max}$. Outside this volume we set $g(x,y,z)=0$.

For a sufficiently low atomic-beam density, only one atom interactions need be considered in calculating photon coincidence spectra [23]. Then, given the presence of one atom uniformly distributed in V_F, the dipole coupling constant distribution is given by

$$P(g)dg=\frac{1}{V_F}dV=\frac{1}{V_F}\left|\frac{dV}{dg}\right|dg, \quad g\geq Fg_{\max}, \tag{A4}$$

where $dV=V(g-dg)-V(g)$. In the following we evaluate the explicit form of this distribution, first without further confining the atomic beam in the (y,z) plane, then in the presence of a (y,z)-plane mask.

1. Without a (y,z)-plane mask

We must find an explicit expression for $|dV/dg|$. Using the periodicity along the cavity axis, we write

$$V(g)=MV_0(g) \tag{A5}$$

with

$$V_0(g)=\{(x,y,z):x^2+y^2\leq w_0^2\ln[g_{\max}\cos(kz)/g],$$
$$|z|\leq k^{-1}\cos^{-1}(g/g_{\max})\}. \tag{A6}$$

Then,

$$\begin{aligned}V(g)&=M4\pi\int_0^{k^{-1}\cos^{-1}(g/g_{\max})}dz\int_0^{w_0\sqrt{\ln[g_{\max}\cos(kz)/g]}}r\,dr\\&=M\lambda w_0^2\int_0^{\cos^{-1}(g/g_{\max})}d\theta\,\ln(g_{\max}\cos\theta/g)\\&=M\lambda w_0^2\int_0^{\cos^{-1}(g/g_{\max})}d\theta\,\theta\tan\theta,\end{aligned}$$

where $\theta=kz$, and the final line follows after integrating by parts. With the change of variable $\cos\theta=\xi$, we obtain

$$V(g)=M\lambda w_0^2\int_{g/g_{\max}}^1 d\xi\frac{\cos^{-1}\xi}{\xi}, \tag{A7}$$

and differentiation with respect to g gives

$$\left|\frac{dV}{dg}\right|=M\lambda w_0^2\frac{\cos^{-1}(g/g_{\max})}{g} \tag{A8}$$

and

$$V_F=M\lambda w_0^2\int_F^1 d\xi\frac{\cos^{-1}\xi}{\xi}. \tag{A9}$$

The coupling constant distribution follows from Eqs. (A4), (A8), and (A9).

2. With a (y,z)-plane mask

We now consider an atomic beam whose transverse profile is confined by a (y,z)-plane mask. Figure 9 illustrates the

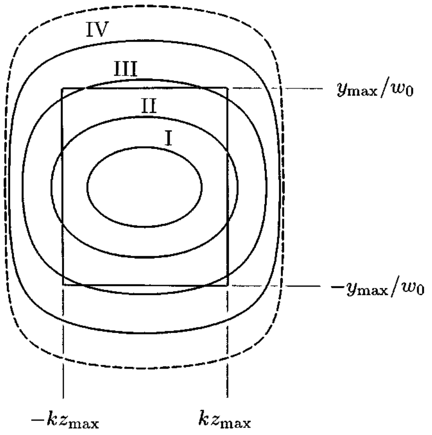

FIG. 9. (y,z)-plane mask with four overlayed contours $g(0,y,z)=g$. Each contour is labeled by the range of g, as defined in the text, within which it lies. The dashed line is the cutoff contour $g(0,y,z)=Fg_{\max}$. The mask repeats, periodically, at each antinode of the standing wave.

rectangular mask, overlayed by four contours, $g(0,y,z)=g$, of constant dipole coupling strength. The mask is defined by the choice of two numbers, $y_{\max}/w_0$ and $kz_{\max}$. The four contours define four distinct ranges of g, differentiated by the way in which each contour either crosses, or does not cross, the rectangular boundary of the mask. Crossings occur according to the sequence shown in Fig. 9 if

$$\cos(kz_{\max})>\max[e^{-y_{\max}^2/w_0^2},Fe^{y_{\max}^2/w_0^2}]. \tag{A10}$$

This condition imposes stronger confinement of the atomic beam in the z direction than the y direction (as g decreases contours intersect $z=\pm z_{\max}$ before $y=\pm y_{\max}$). It also requires the complete mask boundary to fall within the cutoff contour $g(0,y,z)=Fg_{\max}$. Choices of $y_{\max}$ and $z_{\max}$ which do not satisfy inequality (A10) call for a different partitioning into distinct ranges of g. While our derivation of $|dV/dg|$ assumes the partition defined by Fig. 9, it is readily generalized to treat other cases.

In the presence of the (y,z)-plane mask the interaction volume V_F is given be Eqs. (A3) and (A5) with

$$V_0(Fg_{\max})=\{(x,y,z):x^2\leqslant w_0^2\ln[\cos(kz)/F]-y^2,$$
$$|y|\leqslant y_{\max},|z|\leqslant z_{\max}\}. \tag{A11}$$

An explicit expression for V_F appears below as Eq. (A21). The explicit calculation of $V(g)$, and hence $|dV/dg|$, proceeds in a slightly different way in each of the four distinct ranges of g.

a. Range I: $1\geqslant g/g_{max}\geqslant\cos(kz_{max})$

Here the contour $g(0,y,z)=g$ lies entirely within the rectangular mask boundary. The volume enclosed by the surface $g(x,y,z)=g$ is given by Eqs. (A5) and (A6), and $|dV/dg|$ is calculated exactly as before. In Range I the dipole coupling constant distribution is given by Eqs. (A4), (A8), and (A21).

b. Range II: $\cos(kz_{max})>g/g_{max}\geqslant e^{-y_{max}^2/w_0^2}$

In this range the contour $g(0,y,z)=g$ crosses the mask boundary at $|z|=z_{\max}$. The interaction volume includes only that part of the volume enclosed by $g(x,y,z)=g$ which is visible through the mask; in place of Eq. (A6) we have

$$V_0(g)=\{(x,y,z):x^2+y^2\leqslant w_0^2\ln[g_{\max}\cos(kz)/g],\ |z|\leqslant z_{\max}\}, \tag{A12}$$

where the only change is the restricted range of z. The calculation of $|dV/dg|$ follows as before to give

$$\left|\frac{dV}{dg}\right|=M\lambda w_0^2\frac{kz_{\max}}{g}. \tag{A13}$$

In Range II the dipole coupling constant distribution is given by Eqs. (A4), (A13), and (A21).

c. Range III: $e^{-y_{max}^2/w_0^2}>g/g_{max}\geqslant\cos(kz_{max})e^{-y_{max}^2/w_0^2}$

In this small range of g the contour $g(0,y,z)=g$ crosses all four sides of the mask boundary. The volume $V(g)$ is given by Eq. (A5) and

$$V_0(g)=\{(x,y,z):x^2\leqslant w_0^2\ln[g_{\max}\cos(kz)/g]-y^2,$$
$$|y|\leqslant\min(y_{\max},w_0\sqrt{\ln[g_{\max}\cos(kz)/g]}),|z|\leqslant z_{\max}\}. \tag{A14}$$

This volume is no longer cylindrically symmetric and its explicit expression becomes more complex. In particular, the integral over z must be separated into two parts. We have

$$\begin{aligned}V(g)=&M8\int_0^{k^{-1}\cos^{-1}(ge^{y_{\max}^2/w_0^2}/g_{\max})}dz\int_0^{y_{\max}}dy\int_0^{\sqrt{w_0^2\ln[g_{\max}\cos(kz)/g]-y^2}}dx\\&+M8\int_{k^{-1}\cos^{-1}(ge^{y_{\max}^2/w_0^2}/g_{\max})}^{z_{\max}}dz\int_0^{w_0\sqrt{\ln[g_{\max}\cos(kz)/g]}}dy\int_0^{\sqrt{w_0^2\ln[g_{\max}\cos(kz)/g]-y^2}}dx\\=&M\lambda\frac{4}{\pi}\int_0^{\cos^{-1}(ge^{y_{\max}^2/w_0^2}/g_{\max})}d\theta\int_0^{y_{\max}}dy\sqrt{w_0^2\ln(g_{\max}\cos\theta/g)-y^2}\\&+M\lambda w_0^2\frac{4}{\pi}\int_{\cos^{-1}(ge^{y_{\max}^2/w_0^2}/g_{\max})}^{kz_{\max}}d\theta\ln(g_{\max}\cos\theta/g)\int_0^{\pi/2}d\eta\cos^2\eta,\end{aligned} \tag{A15}$$

where we have made the change of variable $\sin\eta = y/w_0\sqrt{\ln[g_{\max}\cos(kz)/g]}$ and, as before, $\theta = kz$. Performing the second integral in the manner used to reach Eq. (A7), we obtain

$$V(g)=M\lambda\,\frac{4}{\pi}\int_0^{\cos^{-1}(ge^{y^2_{\max}/w_0^2}/g_{\max})}d\theta\int_0^{y_{\max}}dy\,\sqrt{w_0^2\ln(g_{\max}\cos\theta/g)-y^2}+M\lambda\,w_0^2\left\{kz_{\max}\ln\left[\frac{g_{\max}\cos(kz_{\max})}{g}\right]\right.$$
$$\left.-\frac{y^2_{\max}}{w_0^2}\cos^{-1}\left(\frac{ge^{y^2_{\max}/w_0^2}}{g_{\max}}\right)+\int_{\cos(kz_{\max})}^{ge^{y^2_{\max}/w_0^2}/g_{\max}}d\xi\,\frac{\cos^{-1}\xi}{\xi}\right\}. \tag{A16}$$

Then

$$\left|\frac{dV}{dg}\right|=M\lambda\,w_0^2\left\{\frac{4}{\pi}\,\frac{1}{w_0^2}\,\frac{e^{y^2_{\max}/w_0^2}/g_{\max}}{\sqrt{1-(ge^{y^2_{\max}/w_0^2}/g_{\max})^2}}\int_0^{y_{\max}}dy\,\sqrt{y^2_{\max}-y^2}\right.$$
$$+\frac{2}{\pi}\,\frac{1}{g}\int_0^{\cos^{-1}(ge^{y^2_{\max}/w_0^2}/g_{\max})}d\theta\int_0^{y_{\max}}dy\frac{1}{\sqrt{w_0^2\ln(g_{\max}\cos\theta/g)-y^2}}$$
$$\left.+\frac{1}{g}\left[kz_{\max}-\cos^{-1}\left(\frac{ge^{y^2_{\max}/w_0^2}}{g_{\max}}\right)\right]-\frac{y^2_{\max}}{w_0^2}\,\frac{e^{y^2_{\max}/w_0^2}/g_{\max}}{\sqrt{1-(ge^{y^2_{\max}/w_0^2}/g_{\max})^2}}\right\}$$
$$=M\lambda\,w_0^2\frac{1}{g}\left\{kz_{\max}-\cos^{-1}\left(\frac{ge^{y^2_{\max}/w_0^2}}{g_{\max}}\right)+\frac{2}{\pi}\int_0^{\cos^{-1}(ge^{y^2_{\max}/w_0^2}/g_{\max})}d\theta\,\sin^{-1}\left[\frac{y_{\max}}{w_0\sqrt{\ln(g_{\max}\cos\theta/g)}}\right]\right\}. \tag{A17}$$

In Range III the dipole coupling constant distribution is given by Eqs. (A4), (A17), and (A21).

d. Range IV: $\cos(kz_{\max})e^{-y^2_{\max}/w_0^2} > g/g_{\max} \geq F$

The contour $g(0,y,z)=g$ lies entirely outside the rectangular mask boundary; $V(g)$ is given by Eq. (A5) and

$$V_0(g)=\{(x,y,z):x^2\leq w_0^2\ln[g_{\max}\cos(kz)/g]-y^2,|y|\leq y_{\max},|z|\leq z_{\max}\}. \tag{A18}$$

The first term of Eq. (A15) now covers the complete integration range in z

$$V(g)=M\lambda\,\frac{4}{\pi}\int_0^{kz_{\max}}d\theta\int_0^{y_{\max}}dy\,\sqrt{w_0^2\ln(g_{\max}\cos\theta/g)-y^2}. \tag{A19}$$

Thus,

$$\left|\frac{dV}{dg}\right|=M\lambda\,w_0^2\,\frac{2}{\pi}\,\frac{1}{g}\int_0^{kz_{\max}}d\theta\int_0^{y_{\max}}dy\,\frac{1}{\sqrt{w_0^2\ln(g_{\max}\cos\theta/g)-y^2}}$$
$$=M\lambda\,w_0^2\,\frac{2}{\pi}\,\frac{1}{g}\int_0^{kz_{\max}}d\theta\,\sin^{-1}\left[\frac{y_{\max}}{w_0\sqrt{\ln(g_{\max}\cos\theta/g)}}\right]. \tag{A20}$$

In Range IV the dipole coupling constant distribution is given by Eqs. (A4), (A20), and the interaction volume V_F which now follows from Eqs. (A3) and (A5)

$$V_F=M\lambda\,\frac{4}{\pi}\int_0^{kz_{\max}}d\theta\int_0^{y_{\max}}dy\,\sqrt{w_0^2\ln(\cos\theta/F)-y^2}$$
$$=M\lambda\,w_0^2\,\frac{4}{\pi}\int_0^{kz_{\max}}d\theta\,\ln(\cos\theta/F)\int_0^{\sin^{-1}[y_{\max}/w_0\sqrt{\ln(\cos\theta/F)}]}d\eta\,\cos^2\eta$$
$$=M\lambda\,w_0^2\,\frac{2}{\pi}\int_0^{kz_{\max}}d\theta\left\{\ln(\cos\theta/F)\sin^{-1}\left[\frac{y_{\max}}{w_0\sqrt{\ln(\cos\theta/F)}}\right]+\frac{y_{\max}}{w_0}\sqrt{\ln(\cos\theta/F)-\frac{y^2_{\max}}{w_0^2}}\right\}. \tag{A21}$$

[1] E. T. Jaynes and F. W. Cummings, Proc. IEEE **51**, 89 (1963).
[2] H. Paul, Ann. Phys. (N.Y.) **11**(7), 411 (1963).
[3] H. I. Yoo and J. H. Eberly, Phys. Rep. **118**, 239 (1985).
[4] B. Shore and P. L. Knight, J. Mod. Opt. **40**, 1195 (1993).
[5] H. M. Gibbs, Phys. Rev. A **8**, 446 (1973); **8**, 456 (1973).
[6] L. Mandel, in *Progress in Optics*, edited by E. Wolf (North-Holland, Amsterdam, 1976), Vol. XII, pp. 27–68.
[7] C. R. Stroud, Jr. and E. T. Jaynes, Phys. Rev. A **1**, 106 (1970).
[8] E. T. Jaynes, in *Coherence and Quantum Optics*, edited by L. Mandel and E. Wolf (Plenum, New York, 1973), pp. 35–68.
[9] J. S. Bell, Physics **1**, 195 (1964).
[10] J. S. Bell, Rev. Mod. Phys. **38**, 447 (1966).
[11] G. Rempe, H. Walther, and N. Klein, Phys. Rev. Lett. **58**, 353 (1987).
[12] M. Brune, F. Schmidt-Kaler, A. Maali, J. Dreyer, E. Hagley, J. M. Raimond, and S. Haroche, Phys. Rev. Lett. **76**, 1800 (1996).
[13] M. G. Raizen, R. J. Thompson, R. J. Brecha, H. J. Kimble, and H. J. Carmichael, Phys. Rev. Lett. **63**, 240 (1989).
[14] Y. Zhu, D. J. Gauthier, S. E. Morin, Q. Wu, H. J. Carmichael, and T. W. Mossberg, Phys. Rev. Lett. **64**, 2499 (1990).
[15] R. J. Thompson, G. Rempe, and H. J. Kimble, Phys. Rev. Lett. **68**, 1132 (1992).
[16] C. Weisbuch, M. Nishioka, A. Ishikawa, and Y. Arakawa, Phys. Rev. Lett. 69, 3314 (1992).
[17] G. Khitrova, K. Tai, E. K. Lindmark, T. R. Nelson, Jr., D. V. Wick, J. D. Berger, O. Lyngnes, J. Prineas, S. Park, H. M. Gibbs, and Y. Lai (unpublished).
[18] T. B. Norris, J.-K. Rhee, C.-Y. Sung, Y. Arakawa, M. Nishioka, and C. Weisbuch, Phys. Rev. B **50**, 14 663 (1994).
[19] H. Wang, J. Shah, T. C. Damen, W. Y. Jan, J. E. Cunningham, M. Hong, and J. P. Mannaerts, Phys. Rev. B **51**, 14 713 (1994).
[20] J. Jacobson, S. Pau, H. Cao, G. Björk, and Y. Yamamoto, Phys. Rev. A 51, 2542 (1995).
[21] H. Wang, J. Shah, T. C. Damen, L. N. Pfeiffer, and J. E. Cunningham, Phys. Status Solidi B **188**, 38 (1995).
[22] R. Houdré, J. L. Gibernon, P. Pellandini, R. P. Stanley, U. Oesterle, C. Weisbuch, J. O'Gorman, B. Roycroft, and M. Ilegems, Phys. Rev. B **52**, 7810 (1995).
[23] H. J. Carmichael, P. Kochan, and B. C. Sanders, Phys. Rev. Lett. **77**, 631 (1996).
[24] B. C. Sanders and H. J. Carmichael, in *CLEO/Pacific Rim '95*, The Pacific Rim Conference on Lasers and Electro-Optics Technical Digest, Makuhari Messe Convention Center, 1995 (Institute of Electrical and Electronics Engineers, Piscataway, NJ, 1995), pp. 243, 244.
[25] D. Meschede, H. Walther, and G. Müller, Phys. Rev. Lett. **54**, 551 (1985).
[26] A. N. Khovanskii, *The Application of Continued Fractions and Their Generalizations to Problems in Approximation Theory* (Noordhoff, Groningen, 1963), pp. 1–9.
[27] H. Risken, *The Fokker-Planck Equation: Methods of Solution and Applications* (Springer-Verlag, Berlin, 1984), Chap. 9.
[28] H. J. Kimble, O. Carnal, N. Georgiades, H. Mabuchi, E. S. Polzik, R. J. Thompson, and Q. A. Turchette, *Atomic Physics 14*, Fourteenth International Conference on Atomic Physics, edited by D. J. Wineland, C. E. Wieman, and S. J. Smith, AIP Conf. Proc. No. 323 (AIP, New York, 1995), pp. 314–335.
[29] L. Tian and H. J. Carmichael, Phys. Rev. A **46**, R681 (1992).